Supporting Information

Donovan et al. 10.1073/pnas.1218528110

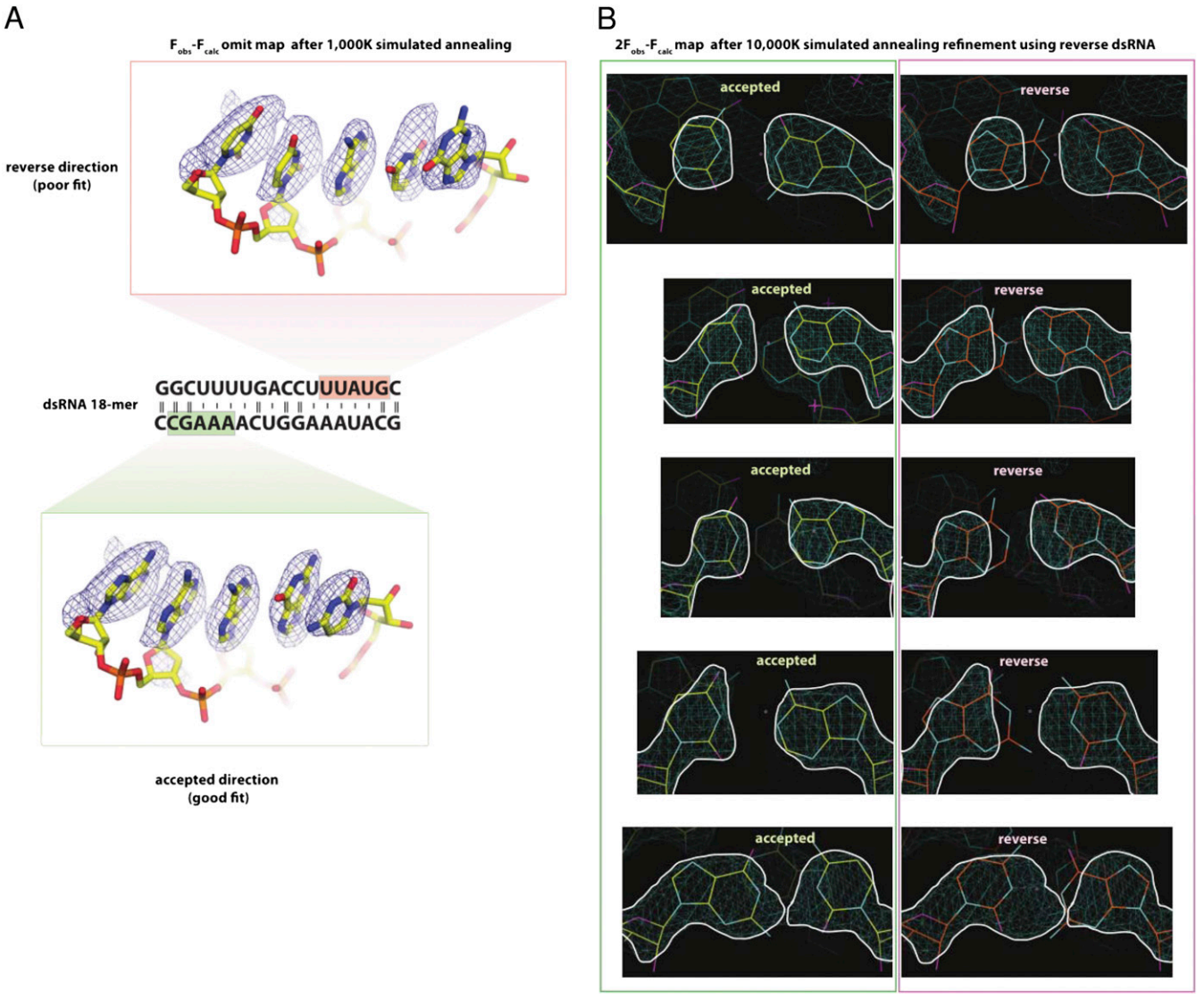

Fig. S1. Confirmation of the dsRNA position in the hOAS1•dsRNA•dATP complex. (*A*) The double-stranded RNA (dsRNA) bound to the human sensor of dsRNA oligoadenylate synthetase 1 (hOAS1) could be modeled into the electron density map in two symmetrical orientations. The correct orientation is determined unambiguously from the omit map $F_{obs} - F_{calc}$ calculated using simulated-annealing (starting at 1,000 K) refined model. Contour level is 3σ. Nucleobases shown were deleted before the refinement. (*B*) Assigning the dsRNA direction by invalidating the reverse model. Here, dsRNA was modeled in reverse direction and the resulting structure was refined using simulated annealing starting at 10,000 K. The resulting biased map $2F_{obs} - F_{calc}$ contoured at 3σ is shown. This procedure introduces bias for the reverse orientation of dsRNA; however, the electron density still unambiguously represents forward dsRNA sequence. Notably, R_{free} increased from 0.2827 to 0.2983, further indicating that the reverse orientation is less consistent with the diffraction data than the forward orientation.

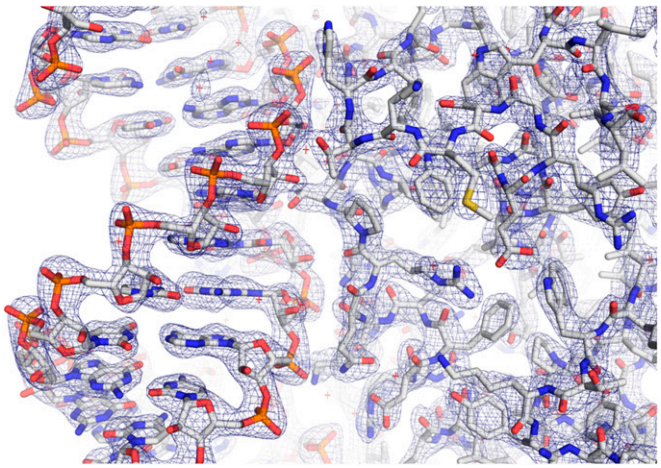

Fig. S2. Electron density for the hOAS1•dsRNA•dATP complex. The $2F_{obs} - F_{calc}$ map for the protein/RNA interface calculated using simulated-annealing refined model (starting temperature 2,000 K). The map is contoured at 2σ.

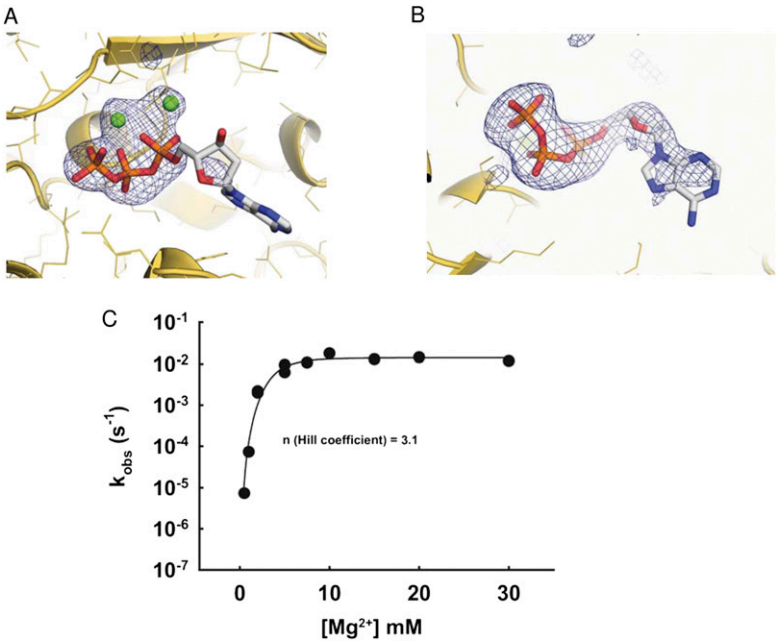

Fig. S3. Two magnesium ions in hOAS1 active site. (*A*) $F_{obs} - F_{calc}$ difference map calculated from the simulated-annealing refined model (starting temperature 2,000 K). 2′-deoxy ATP (dATP) and two magnesium ions were excluded before the refinement. The map is contoured at 4σ. (*B*) Electron density from *A* at contour level 3σ. The structure was rotated relative to *A* to show the sugar and the base. (*C*) Titration of Mg^{2+} reveals cooperativity with Hill coefficient 3.1, consistent with more than one Mg^{2+} ion in the active site of OAS1. The reactions contained 3 μM hOAS1 and 100 μM dsRNA. The data were fit to the Hill equation: $k_{obs} = k_{obs}^{(MAX)} \cdot [Mg^{2+}]^n / ((K_d)^n + [Mg^{2+}]^n)$, where n is Hill coefficient and K_d is an apparent binding affinity of Mg^{2+}. Two magnesium ions were modeled into the electron density based on the following considerations: (*i*) Chemical and physical reasons. We assigned the spherical density in the vicinity of phosphate groups to cations because the density resides between three closely located aspartates and the triphosphate moiety of ATP. Electrostatic repulsion between three negative charges in OAS1 located next to four negative charges on ATP would oppose ATP binding, unless positive ions that neutralize the negative charges were bridging the triphosphate moiety to the protein. (*ii*) Structures of related active sites. Both divalent metal ions have been observed previously in high-resolution structures of nucleotidyl transferases (see PDB codes 2Q66, 1Q79, 4ECZ). (*iii*) Coordination geometry. The coordination geometry of both ions is close to octahedral, consistent with magnesium. Distances between the first Mg^{2+} and protein atoms are 2.0 Å, 2.2 Å, and 2.4 Å, and the second Mg^{2+} and protein are 2.2 Å, 2.6 Å, 2.6 Å, similar to those observed in high-resolution structures of nucleotidyl transferase active sites (PDB codes 2Q66, 1Q79, 4ECZ). (*iv*) Importance of Mg^{2+} for enzymatic activity of OAS1. Using biochemical readout, we show that magnesium is required for 2-5A synthesis (*C*). (*v*) Cooperativity. The presence of two magnesium ions in the crystal structure suggests that the activity of OAS1 may depend on magnesium concentration cooperatively. To test this prediction, we carried out magnesium titration (*C*). The reaction shows a cooperative activation with Hill coefficient $n = 3.1$, consistent with more than one magnesium ion involved in the enzymatic activity. The numeric value 3.1 suggests that OAS1 may use as many as three Mg^{2+} ions. Notably, it has been reported (1) that three magnesium ions (third Mg^{2+} binds transiently) are involved in phosphodiester bond formation in DNA polymerase η that catalyzes a similar chemical reaction of phosphodiester bond synthesis. These considerations together favor placement of two magnesium ions in our model.

1. Nakamura T, Zhao Y, Yamagata Y, Hua YJ, Yang W (2012) Watching DNA polymerase eta make a phosphodiester bond. *Nature* 487(7406):196–201.

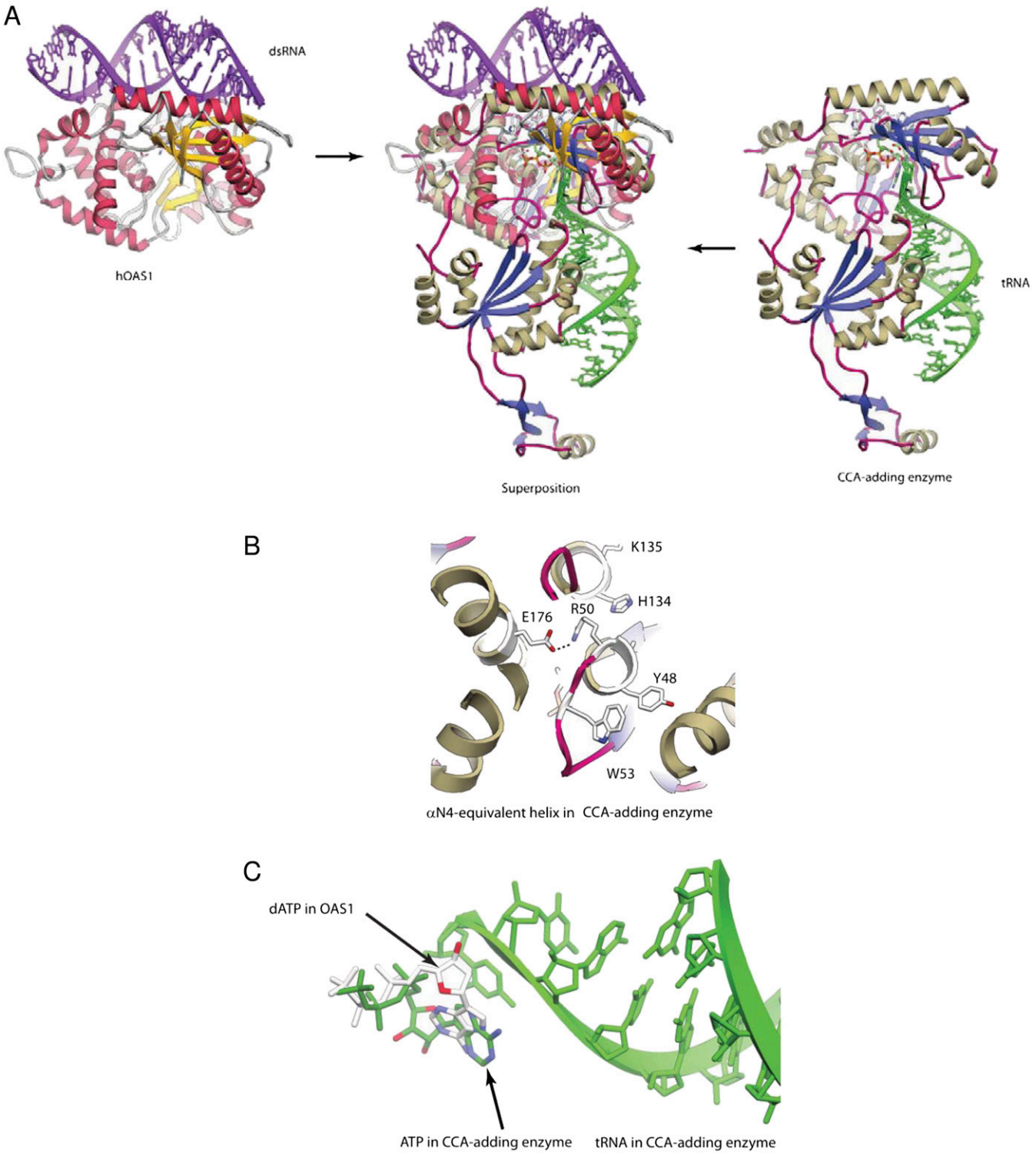

Fig. S4. Comparison of OAS1 with CCA-adding enzyme. (*A*) Superposition of hOAS1 and CCA-adding enzyme (PDB code 1TFW) with bound RNA. (*B*) Structure of the RNA-induced catalytic structure (RICS)-equivalent region in CCA-adding enzyme. (*C*) Comparison of nucleotide binding in the active sites of hOAS1 and CCA-adding enzyme. Superposition was obtained by aligning the active site residues in both enzymes.

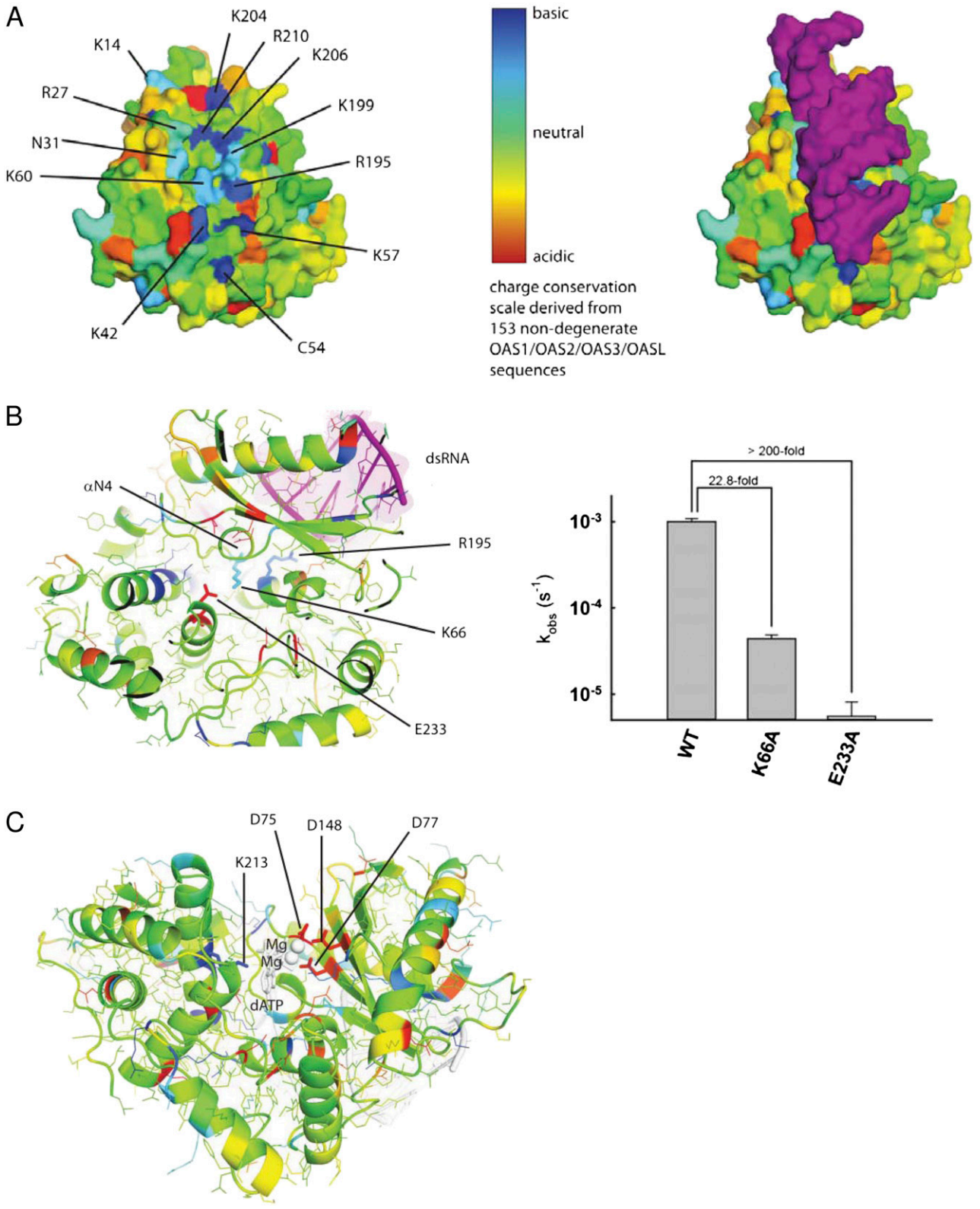

Fig. S5. Charge conservation in oligoadenylate synthetases. (*A*) Conservation of surface charges on the dsRNA-binding surface mapped onto hOAS1. The coloring scheme is annotated on the included scale. dsRNA masks nearly all conserved basic residues. (*B*, *Left*) Conservation of the K66/R195/E233 switch. (*Right*) Effects of K66A and E233A mutations on OAS1 activity in the presence of dsRNA. Measurements were conducted as in Fig. 2*C*. Error bars show SEs from two independent experiments. For the E233A mutant the 2-5A product was not detected and the bar represents an upper rate limit estimated from the background signal. (*C*) Conservation of the active site triad, D75/D77/D148, and of the ATP-binding residue K213. Multiple sequence alignment, computation of charge conservation and PDB file were prepared in SEQMOL-K_d (http://biochemlabsolutions.com/FASTAandPDB.html). The structures were visualized in PyMol 1.2 (DeLano Scientific).

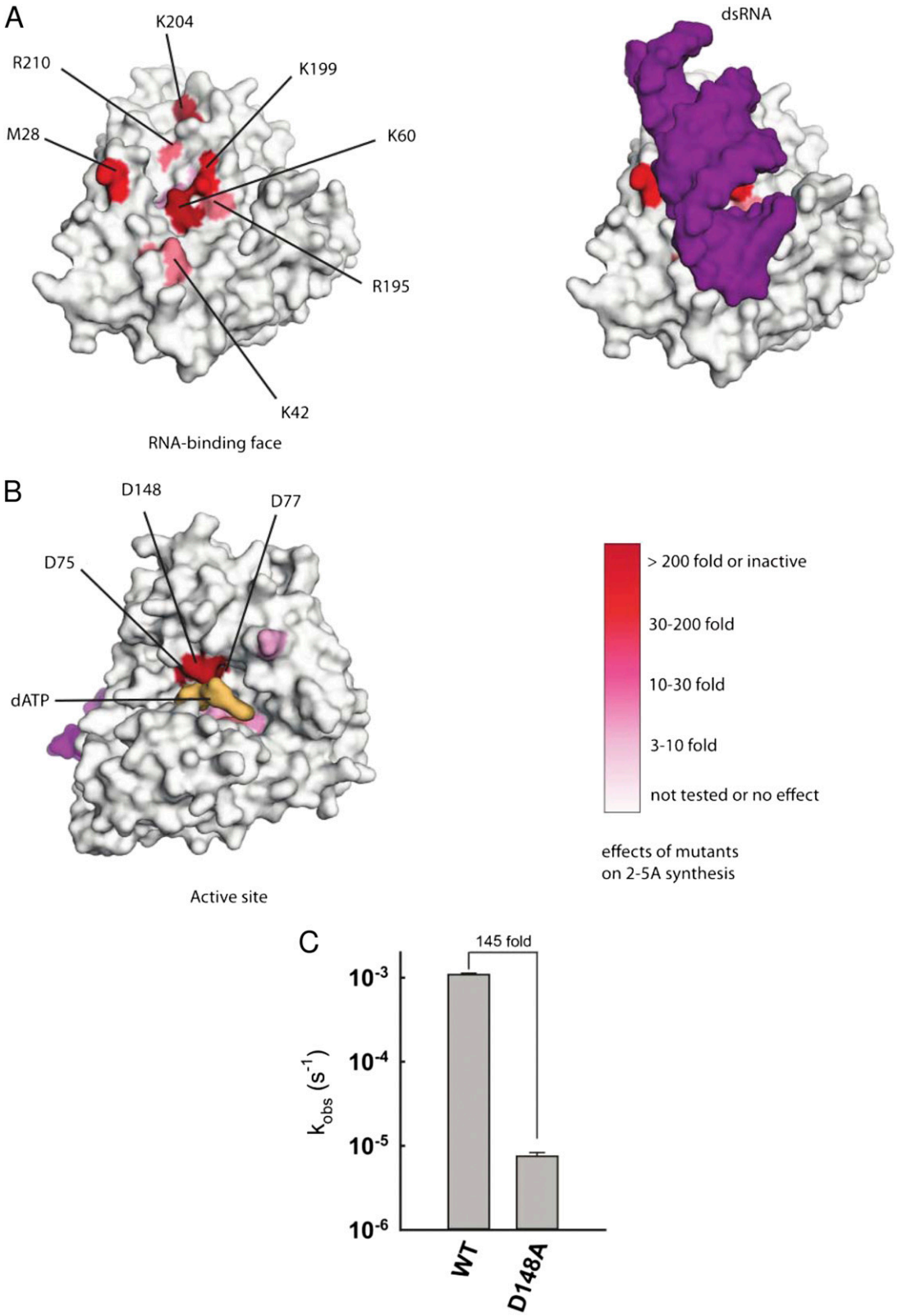

Fig. S6. Effects of point mutants on activity of OAS1 (1–3). (*A*) Effects of mutations that map to the dsRNA binding surface. (*B*) Effects of mutations that map to the active site. The figure was generated in PyMol 1.2 (DeLano Scientific). (*C*) The effect of D148A mutant on hOAS1 activity measured in this work.

1. Hartmann R, Justesen J, Sarkar SN, Sen GC, Yee VC (2003) Crystal structure of the 2′-specific and double-stranded RNA-activated interferon-induced antiviral protein 2′-5′-oligoadenylate synthetase. *Mol Cell* 12(5):1173–1185.
2. Sarkar SN, et al. (2005) Natural mutations in a 2′-5′ oligoadenylate synthetase transgene revealed residues essential for enzyme activity. *Biochemistry* 44(18):6837–6843.
3. Torralba S, Sojat J, Hartmann R (2008) 2′-5′ oligoadenylate synthetase shares active site architecture with the archaeal CCA-adding enzyme. *Cell Mol Life Sci* 65(16):2613–2620.

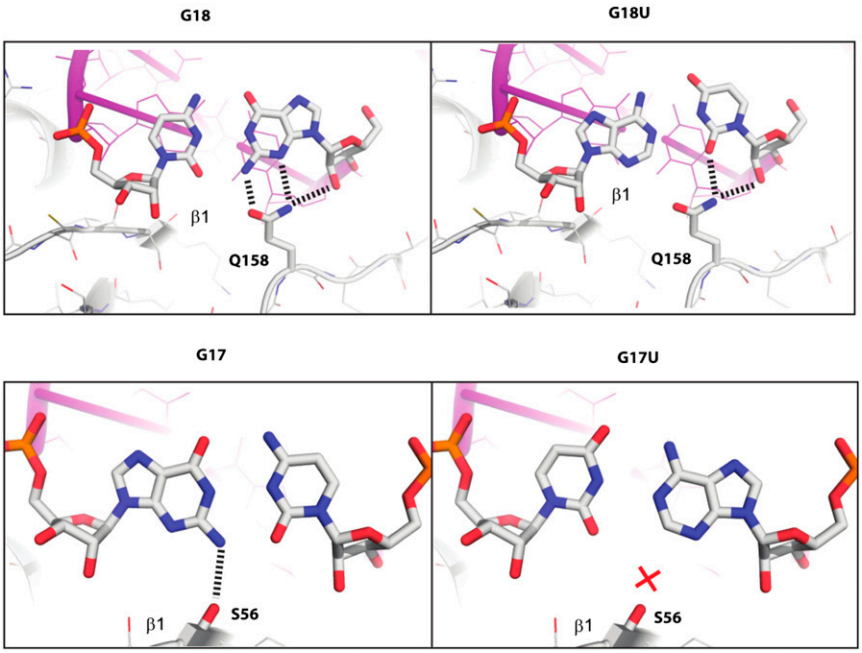

Fig. S7. Hydrogen bonding interactions of G17 and G18 nucleobases compared with hydrogen bonding interactions upon GC18UA and GC17UA mutations. The modeling of RNA mutants was done in coot (1).

1. Emsley P, Cowtan K (2004) Coot: Model-building tools for molecular graphics. *Acta Crystallogr D Biol Crystallogr* 60(Pt 12 Pt 1):2126–2132.

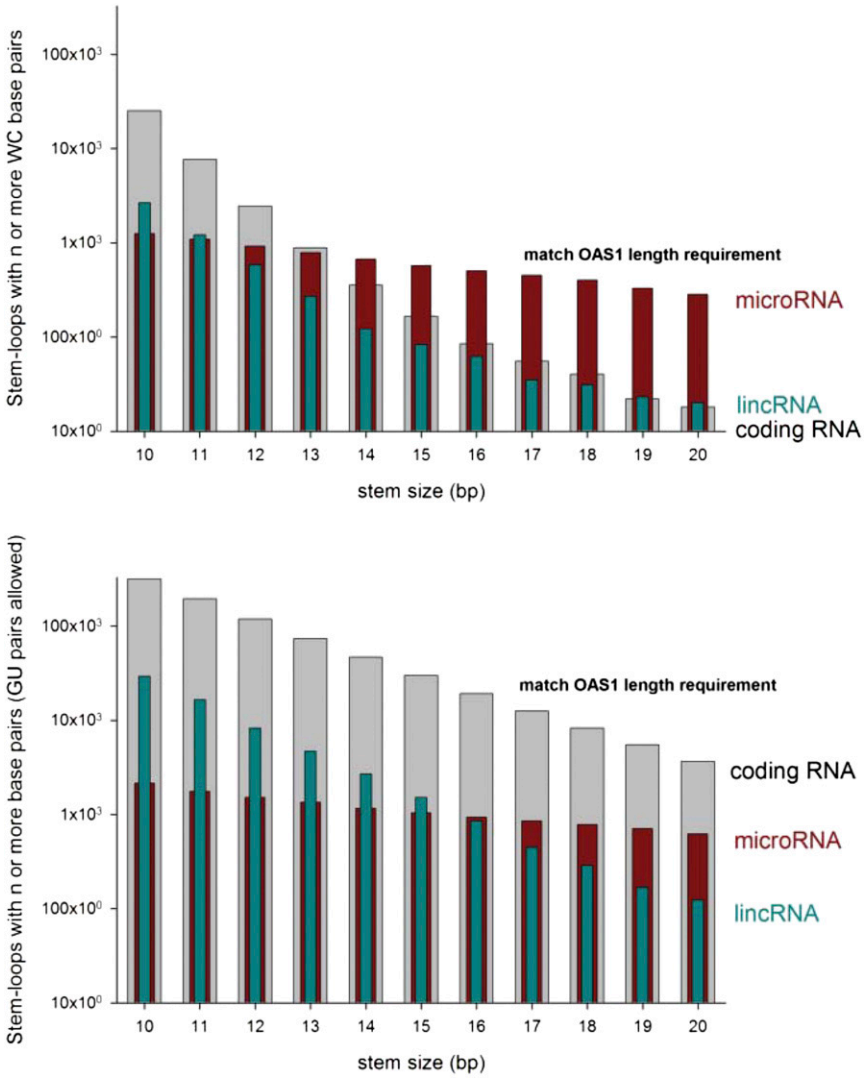

Fig. S8. Distribution of double-stranded RNA sizes in the human genome. The distribution of dsRNA elements in the human genome was calculated by finding local stem-loops with ≤ 150 nucleotides and containing either perfect Watson–Crick stems (*Upper*) or stems with GU pairs allowed (*Lower*). The vertical scale is logarithmic. The RNA sequences were obtained from Ensembl (1) and analyzed using a stem-loop finding algorithm implemented in C# (*SI Text*).

1. Flicek P, et al. (2011) Ensembl 2011. *Nucleic Acids Res* 39(Database issue):D800–D806.

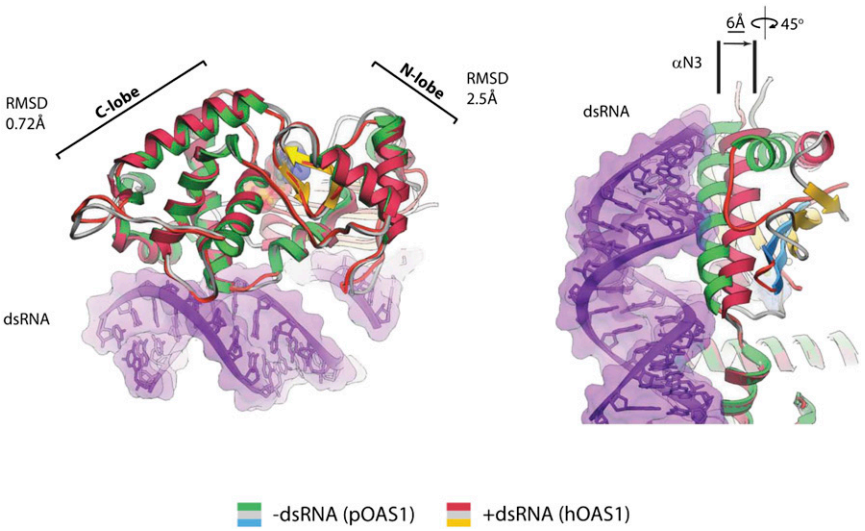

Fig. S9. Superposition of pOAS1 in the inactive conformation (PDB code 1PX5) with hOAS1 in the active conformation (present work). The C lobes are identical in both conformations. dsRNA binding moves helix N3 located at the protein/RNA interface.

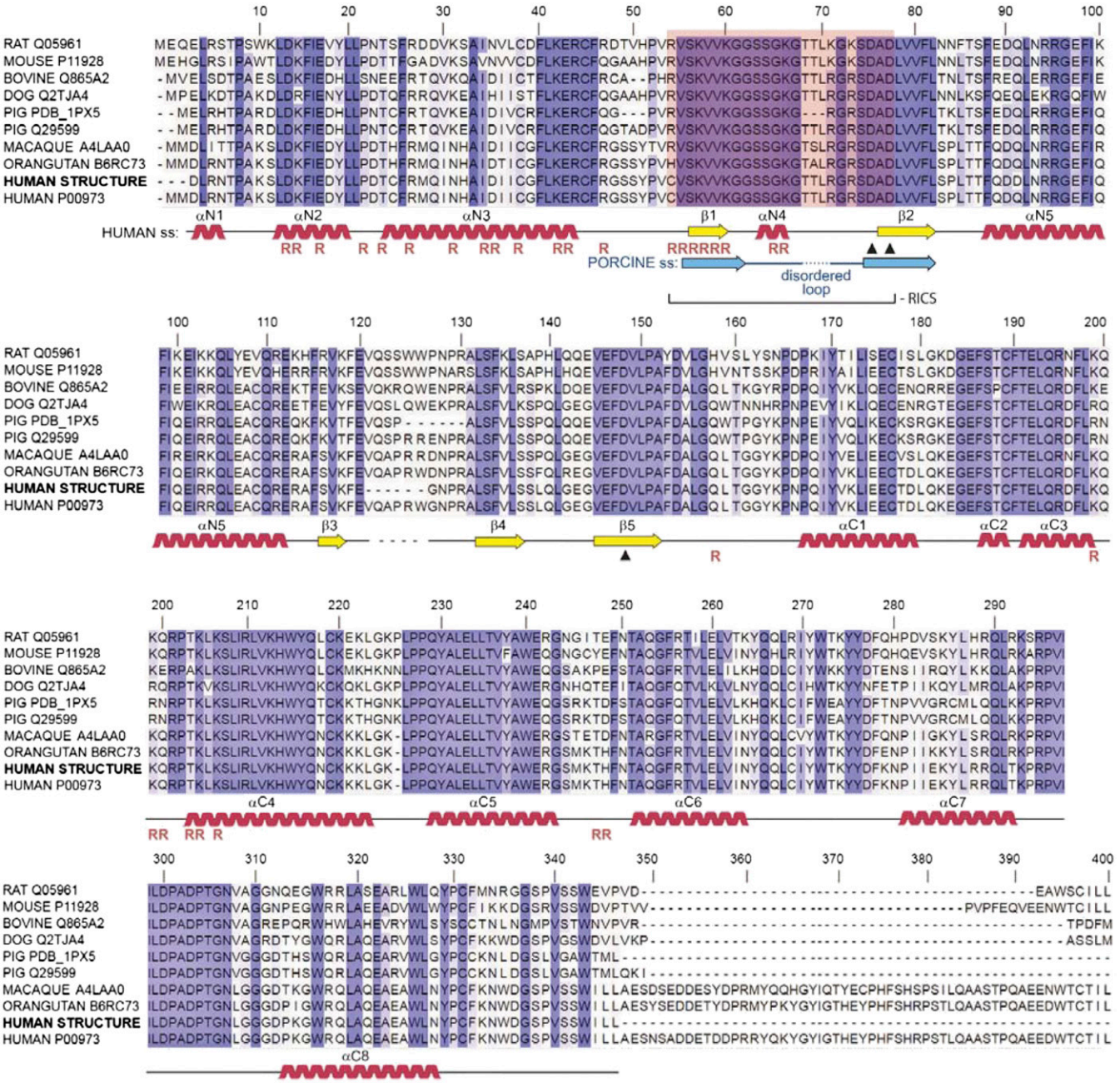

Fig. S10. Multiple sequence alignment of OAS1 including protein sequences from the crystal structures of pOAS1 (PDB code 1PX5) and hOAS1. The R-marks indicate protein/RNA contacts. The filled triangles show the magnesium-coordinating active site residues. Highlighted area shows the RICS comprised of strands β1, β2, helix N4, and the connecting loops. The alignment was generated in SEQMOL-K_d (http://biochemlabsolutions.com/FASTAandPDB.html) and colored in JalView (1).

1. Waterhouse AM, Procter JB, Martin DM, Clamp M, Barton GJ (2009) Jalview Version 2—A multiple sequence alignment editor and analysis workbench. *Bioinformatics* 25(9):1189–1191.

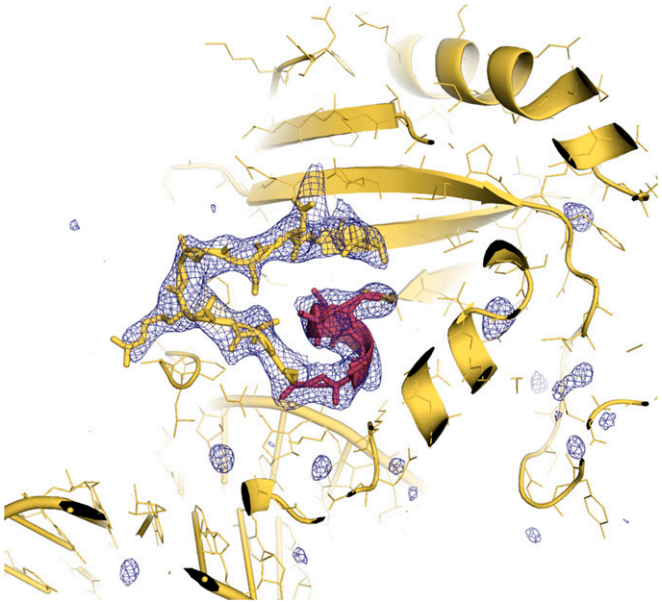

Fig. S11. Electron density map for the helix N4 and the connecting loop in hOAS1. $F_{obs} - F_{calc}$ omit map for the activation switch calculated following simulated annealing (2,000 K). Residues covered by the map were deleted before refinement. The map is contoured at 3σ.

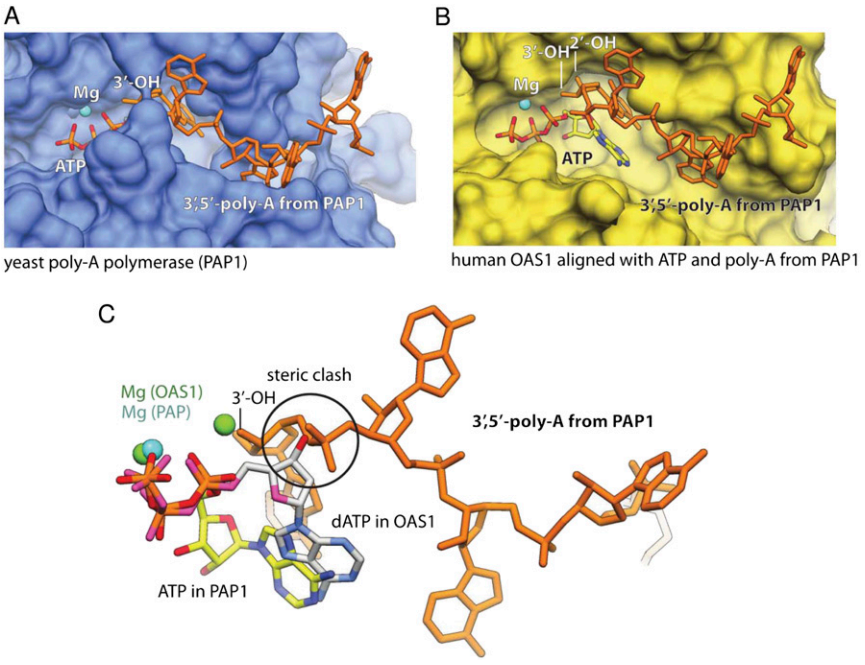

Fig. S12. Comparison of substrate binding in the active sites of hOAS1 and poly-A polymerase (PAP1). (*A*) Surface representation of yeast PAP1 cocrystallized with ATP, magnesium and 3′,5′-poly-A (PDB code 2Q66). (*B*) Surface representation of hOAS1 superimposed with ATP, magnesium and 3′,5′-poly-A product from the PAP1 complex shown in *A*. Superposition was conducted in PyMol 1.2 by aligning the active site and the triphosphate residues in hOAS1 and in PAP1. (*C*) Superposition of dATP bound to hOAS1 with ligands in the active site of PAP1. The sugar moiety of dATP in hOAS1 conflicts with the backbone of the growing 3′,5′-poly-A chain in PAP1.

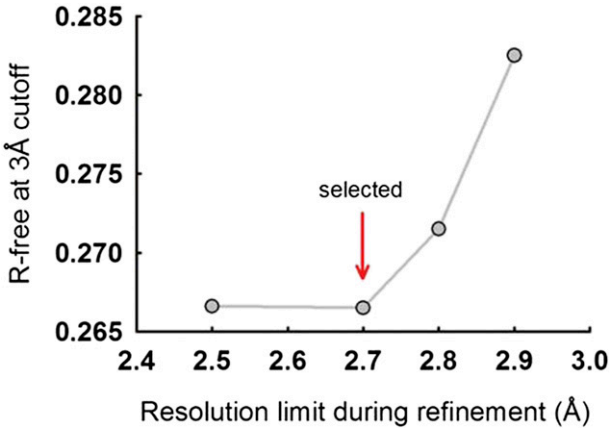

Fig. S13. Model quality at 3 Å cutoff and different refinement resolutions. The final model was rerefined using a series of independent simulated annealing runs (2,000 K) that included all data up to the resolutions shown on the *x* axis. R_{free} was calculated subsequently for each resulting model using a fixed resolution cutoff (3 Å). Retention of the data down to 2.7 Å was necessary to ensure low R_{free}, indicating the appropriate final resolution of the crystal structure.

Table S1. Data collection and refinement statistics

Statistics	Human OAS1•dsRNA•dATP
Data collection	
Space group	$P2_12_12_1$
Cell dimensions	
a, *b*, *c* (Å)	71.2, 93.2, 98.6
α, β, γ (°)	90.0, 90.0, 90.0
Resolution (Å)	67.73–2.7 (2.8–2.7)*
R_{pim} (1)	0.07 (0.466)
CC(1/2) (2)	0.998 (0.906)
$I/\sigma I$	17.15 (2.41)
Completeness (%)	99.9 (99.9)
Redundancy	9.7 (8.5)
Refinement	
Resolution (Å)	2.7
No. unique reflections	18,604 (1,890)
R_{work}/ R_{free}	0.2285/0.2827
No. atoms	
Protein	2,740
dATP	29
Mg	2
dsRNA	756
Water	50
B-factors	
Protein	82.86
dATP	115.86
Mg	86.15
dsRNA	76.01
R.m.s deviations	
Bond lengths (Å)	0.003
Bond angles (°)	0.776
Ramachandran plot (%)	
Favored	90.1
Allowed	9.9
Disallowed	0.0

A single crystal was used for data collection.
*Highest resolution shell is shown in parenthesis.

1. Weiss MS (2001) Global indicators of X-ray data quality. *J Appl Cryst* 34:130–135.
2. Karplus PA, Diederichs K (2012) Linking crystallographic model and data quality. *Science* 336(6084):1030–1033.

Table S2. Comparison of hOAS1 with other dsRNA binding proteins

Parameter	hOAS1	RIG-I	TLR-3	RNase III	Viral STUNT	Viral B2
	IFN response					
Length of dsRNA forming protein/RNA interface (bp)	17	8	44	21	14	17
At least one dsRNA end is capped by protein	N	Y	N	N	Y	N
H-bonds	20	13	15	25	14	8
H-bonds to bases	5	0	4	8	0	2
H-bonds to 2′OH	6	3	7	16	5	4
dASA (Å^2)	−3,042	−3,008	−2,466*	−5,001	−1,822	−1,498
dsRNA distortion (RMSD vs. ideal dsRNA, Å)	2.013	1.150	1.702	1.311	1.680	1.594
PDB accession code	(4IG8)	3TMI (1)	3CIY (2)	2EZ6 (3)	1R9F (4)	1DI2 (5)

bp, base pair; dASA, burial of accessible surface area. dASA values were calculated in SEQMOL-K_d (http://biochemlabsolutions.com/FASTAandPDB.html). The ideal dsRNA was generated in coot (6). The rmsd values were calculated in PyMol 1.2 (DeLano Scientific).
*TLR-3 forms a dimer bridged by dsRNA; the area shown describes the protein/RNA interface of one TLR-3 monomer.

1. Jiang F, et al. (2011) Structural basis of RNA recognition and activation by innate immune receptor RIG-I. *Nature* 479(7373):423–427.
2. Liu L, et al. (2008) Structural basis of toll-like receptor 3 signaling with double-stranded RNA. *Science* 320(5874):379–381.
3. Gan J, et al. (2006) Structural insight into the mechanism of double-stranded RNA processing by ribonuclease III. *Cell* 124(2):355–366.
4. Ye K, Malinina L, Patel DJ (2003) Recognition of small interfering RNA by a viral suppressor of RNA silencing. *Nature* 426(6968):874–878.
5. Ryter JM, Schultz SC (1998) Molecular basis of double-stranded RNA-protein interactions: Structure of a dsRNA-binding domain complexed with dsRNA. *EMBO J* 17(24):7505–7513.
6. Emsley P, Cowtan K (2004) Coot: Model-building tools for molecular graphics. *Acta Crystallogr D Biol Crystallogr* 60(Pt 12 Pt 1):2126–2132.

Other Supporting Information Files

SI Text (DOC)
Dataset S1 (TXT)